In-plane Schottky-barrier field-effect transistors based on 1*T*/2*H* heterojunctions of transition-metal dichalcogenides

Zhi-Qiang Fan,[1,2] Xiang-Wei Jiang,[1,*] Jun-Wei Luo,[1] Li-Ying Jiao,[3] Ru Huang,[4] Shu-Shen Li,[1] and Lin-Wang Wang[5,†]

[1]*Institute of Semiconductors, Chinese Academy of Sciences, Beijing 100083, China*

[2]*School of Physics and Electronic Science, Changsha University of Science and Technology, Changsha 410114, China*

[3]*Key Lab of Organic Optoelectronics & Molecular Engineering, Department of Chemistry, Tsinghua University, Beijing 100084, China*

[4]*Institute of Microelectronics, Peking University, Beijing 100871, China*

[5]*Materials Science Division, Lawrence Berkeley National Laboratory, Berkeley, California 94720, USA*

(Received 18 July 2017; revised manuscript received 7 September 2017; published 2 October 2017; corrected 2 February 2021)

As Moore's law approaches its end, two-dimensional (2D) materials are intensely studied for their potentials as one of the "More than Moore' (MM) devices. However, the ultimate performance limits and the optimal design parameters for such devices are still unknown. One common problem for the 2D-material-based device is the relative weak on-current. In this study, two-dimensional Schottky-barrier field-effect transistors (SBFETs) consisting of in-plane heterojunctions of 1*T* metallic-phase and 2*H* semiconducting-phase transition-metal dichalcogenides (TMDs) are studied following the recent experimental synthesis of such devices at a much larger scale. Our *ab initio* simulation reveals the ultimate performance limits of such devices and offers suggestions for better TMD materials. Our study shows that the Schottky-barrier heights (SBHs) of the in-plane 1*T*/2*H* contacts are smaller than the SBHs of out-of-plane contacts, and the contact coupling is also stronger in the in-plane contact. Due to the atomic thickness of the monolayer TMD, the average subthreshold swing of the in-plane TMD-SBFETs is found to be close to the limit of 60 mV/dec, and smaller than that of the out-of-plane TMD-SBFET device. Different TMDs are considered and it is found that the in-plane WTe_2-SBFET provides the best performance and can satisfy the performance requirement of the sub-10-nm high-performance transistor outlined by the International Technology Roadmap for Semiconductors, and thus could be developed into a viable sub-10-nm MM device in the future.

DOI: 10.1103/PhysRevB.96.165402

I. INTRODUCTION

As the Moore's law based on Si technology is approaching its end, new materials and new designs are intensely studied for their potentials to become "More than Moore" (MM) electronic devices in the future. In the short term, the electronic industry is also looking for technologies for transistors with channel lengths below 10 nm, and thus the International Technology Roadmap for Semiconductors (ITRS) has outlined the performance parameters needed in such devices [1–3]. One very promising approach for MM devices is to use two-dimensional (2D) materials [4–10]. Among different 2D materials, monolayer transition-metal dichalcogenides (TMDs) are very attractive due to their direct band gaps of 1.0–2.0 eV in the 2*H* semiconducting phase, their relative stabilities, and the possibilities for bipolar doping [11–16]. However, there are still some doubts as to whether, ultimately, a single-layer TMD field-effect transistor (FET) can satisfy the ITRS device requirement, especially for its on-state current strength. For example, recent experimental studies indicated that metal/TMD contact poses a major challenge to achieve high-performance transistors [17,18]. In addition, the lattice mismatch between metals and the channel TMD, and possible weak coupling between their electronic states, may impair the efficiency of carrier injection, which leads to small on-state current. Thus, how to reduce the contact resistance and increase the on-state current beyond that outlined by ITRS for TMD-based devices is a major issue.

Depending on the arrangement of the chalcogen atoms, monolayer TMDs appear in many distinct phases such as the 2*H* phase, 1*T* phase, and distorted 1*T* phase. For a particular TMD, the stabilities of its different phases are not the same [19]. In general, the 2*H* phases of most TMDs are more stable than the others thermodynamically [20–22]. For example, the formation energy of the 1*T* phases of MoS_2 is 0.84 per formula unit higher than that of the 2*H* phase [22]. On the other hand, related theoretical studies have suggested that the energetically more stable phase is a distorted 2×1 reconstruction of the 1*T* phase [23–25]. However, recent experiments demonstrate that the 2*H* phase TMDs can transit to the 1*T* phase with the help of chemical modification [26]. A semiconductor-to-metal transition accompanies these 2*H* to 1*T* structural changes [27–29]. More excitingly, the in-plane (IP) 1*T*/2*H* heterojunctions of MoS_2 and WSe_2 have been fabricated to form phase-engineered low-resistance contacts transistors [30–32]. It has shown that the IP 1*T*/2*H* heterojunction transistors have much better performances than the more traditional 2*H*/metal contact transistors [30–32]. However, the experimental device at the current stage is at the scale of μm, instead of nm, and uses multiple-layer TMD instead of single layer. It will thus be extremely useful to study the following: what is the ultimate limit in an ideal device when it is shrunk to less than 10 nm and with single-layer TMD; what is the best TMD material to choose to have the best performance; and what is the determining factor for such a device? *Ab initio* calculations and device simulations can help to address these critical questions.

*xwjiang@semi.ac.cns

†lwwang@lbl.gov

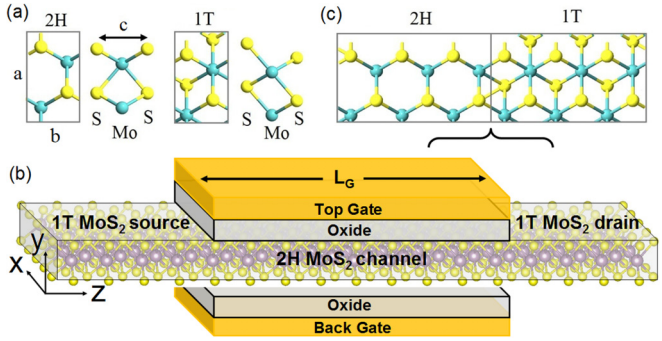

FIG. 1. (a) Atomic structures of MoS_2 rectangular unit cells with $2H$ and $1T$ phases. (b) The schematic structure of double-gated SBFET based on $1T$-$2H$-$1T$ monolayer MoS_2. (c) The schematic $2H/1T$ interface of MoS_2.

The IP $1T/2H$ contact is also of great fundamental interest due to the absence of interface defect, which can cause Fermi-level pinning. Important questions include the following: What determines the band alignment at an IP $1T/2H$ contact? Is that determined by their alignments to the vacuum, as was found for vertical out-of-plane (OP) contacts [13]? Besides, what is the nature of the IP $1T/2H$ contact itself? We found that the IP contact is a Schottky-barrier contact and, as a result, the device is a monolayer Schottky-barrier field-effect transistor (SBFET). Quantum transport simulations based on density functional theory (DFT) and the nonequilibrium Green's function (NEGF) method will be used to study these physical problems and to simulate the whole device I/V curve. We will also compare an IP contact device with the OP contact device with the same conductive $1T$ phase electrode. It is found that with the proper choice of the $1T$ phase materials (e.g., WTe_2), it is possible to have the on-state current be larger than the ITRS-outlined requirement for sub-10-nm devices. It is also found that the IP $1T/2H$ heterostructure device is indeed superior to the OP contact devices, which is consistent with the experimental observations.

II. MODEL AND SIMULATION APPROACH

We choose six TMD materials, $MX_2 (M = \text{Mo, W}; X = \text{S, Se, Te})$, in our current study. The $1T$-MoS_2 and $2H$-MoS_2 are used here as our example. Figure 1(a) shows the atomic structures of MoS_2 rectangular unit cells in semiconducting ($2H$) and metallic ($1T$) phases. The device of a double-gated SBFET based on $1T$-$2H$-$1T$ monolayer MoS_2 is schematically shown in Fig. 1(b), where the source (S) and drain (D) are metallic $1T$-MoS_2 and the channel is semiconducting $2H$-MoS_2. The channel lengths (L_G) of six SBFETs are all 8.8 nm. The corresponding equivalent oxide thickness (EOT = 0.54 nm) and power supply voltage ($V_{DD} = 0.72$ V) follow the ITRS high performance (HP) requirements. Here, EOT indicates how thick a silicon oxide film would need to be to produce the same effect as the high-k material being used, and V_{DD} is the bias voltage between source and drain. In fact, the previous experimental study showed that the $1T$-MoS_2 and $2H$-MoS_2 could join along their zigzag edges due to the synthesis approach and growth conditions [30]. Experimental measurements and *ab initio* simulations provide a coherent physical picture of the properties of the 2D Schottky junction created at this interface [30]. For comparison, the $1T$-MoS_2 and $2H$-MoS_2 joining along their armchair edges are studied in our paper. The detail atomistic IP $1T/2H$ heterojunction is shown in Fig. 1(c). We see that all the local tetragonal bonds between Mo and S are satisfied without any stretch. Due to the same lattice constants, $1T$-MoS_2 can match with $2H$-MoS_2 very well without any interfacial strains and defects. As a result, the IP $1T/2H$ contacts at the source and drain region are the same as each other.

The device simulations in this work are carried out by using the first-principles software package ATOMISTIX TOOLKIT, which is based on density functional theory in combination with the nonequilibrium Green's function [33]. The exchange-correlation potential is described by the local density approximation (LDA) and the wave function is expanded by the Hartwigsen-Goedecker-Hutter (HGH) basis for all atoms. The k-point samplings for calculations of the bulk's electronic structures and DFT self-consistent calculations of SBFETs are $21 \times 1 \times 21$ and $3 \times 1 \times 100$ in the x, y, and z directions, respectively. $12 \times 1k$-point samplings in the x and y directions for the transmission calculation are the most favorable combination for the sake of more accurate results and saving computational time. The real-space grid techniques are used with the energy cutoff of 200 Ry in numerical integrations. The geometries are optimized until all residual force on each atom is smaller than 0.01 eV Å^{-1}. When a bias voltage is applied, the current $I(V_b)$ can be calculated by the Landauer formula: $I(V_b) = \frac{2e}{h} \int T(E, V_b)[f_L(E, V_b) - f_R(E, V_b)]dE$ [34]. Here, V_b is the bias voltage, $T(E, V_b)$ is the transmission coefficient, and $f_L(E, V_b)$ and $f_R(E, V_b)$ are the Fermi-Dirac distribution functions of the left and right electrodes, respectively.

III. RESULTS AND DISCUSSIONS

Figure 2 shows the calculated band structures of the rectangular unit cells of six TMDs in Fig. 1(a). All $2H$ phases of six TMDs are semiconductors with direct band gaps occurring along the Γ-Z direction, while all $1T$ phases are metals. Table I shows lattice constants of the rectangular cells and the accurate band gaps (E_g) of $2H$-TMDs, which are in good agreement with the experimental measurements and other theoretical calculations [11–16]. We did note the intrinsic band-gap problem of DFT-LDA calculations; however, it is noted by several researchers that for 2D MoS_2 and several other single-layer honeycomb structures, band gaps predicted

TABLE I. Lattice constants of the rectangular cell, the calculated band gaps (E_g) of $2H$-TMDs, as well as IP-Φ_{SB} and OP-Φ_{SB} of six TMD-SBFETs.

Material	a (Å)	b (Å)	c (Å)	E_g(eV)	IP-Φ_{SB} (eV)	OP-Φ_{SB} (eV)
MoS_2	5.474	3.160	3.172	1.795	0.82	0.88
$MoSe_2$	5.695	3.288	3.328	1.598	0.64	0.71
$MoTe_2$	6.094	3.518	3.605	1.195	0.44	0.46
WS_2	5.462	3.153	3.142	1.897	0.85	0.97
WSe_2	5.685	3.282	3.341	1.622	0.68	0.83
WTe_2	6.235	3.601	3.658	1.038	0.35	0.37

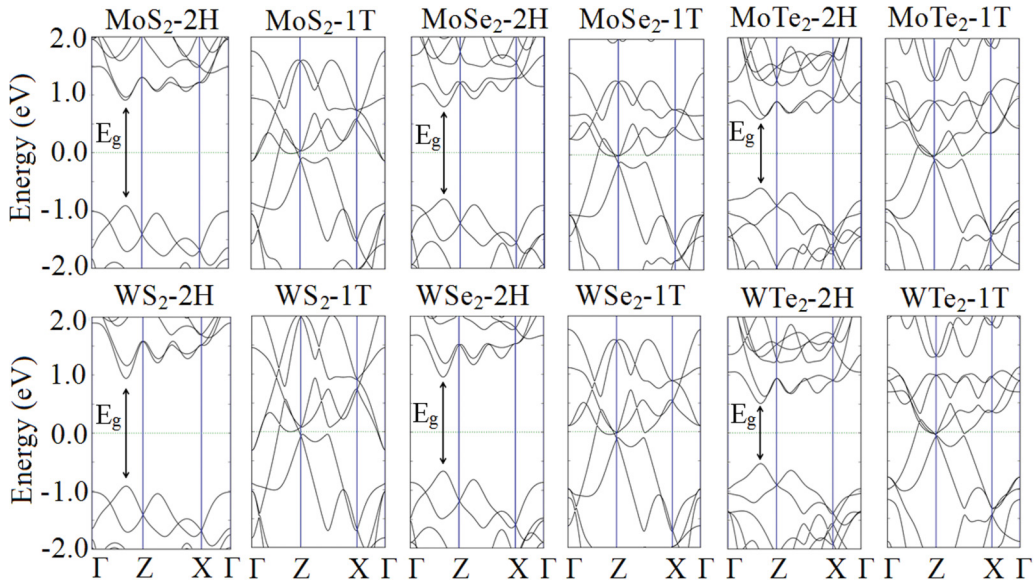

FIG. 2. Band structures of the rectangular unit cells of six TMDs with 2*H* and 1*T* phases. FL is set to zero in the energy scale.

by LDA or PBE results agree better with experimental values than GW, although the physics behind it is not clear [12,19]. The average electron density values along the *Z* direction of six 1*T*-2*H*-1*T* monolayer junctions are demonstrated in Fig. 3. Once the ribbons are joined commensurately, *space-charge regions* form at the boundaries and determine the bending and lineup of band edges. One can see that the fluctuations of the average electron density values at the 1*T*/2*H* interfaces is very small for six IP 1*T*-2*H*-1*T* TMD junctions. It also indicates that the combination along their armchair edges is a good choice for the 1*T*/2*H* heterojunction.

The Schottky-barrier height plays an important role in the transport properties of of SBFETs. Recent theoretical study demonstrates that the linear bending of the band edges of the semiconductor at the boundary between the metal and semiconductor will affect the Schottky-barrier height effectively [35]. Following their method, we calculate the Schottky-barrier height of our devices from the local density states (LDOS), the transmission spectrum, and the averaged potential along the *Z* direction in Figs. 4(a) and 4(b). The junction of the 1*T*-2*H*-1*T*MoS_2 is used here as our example. First, we determine the energy difference between the Fermi

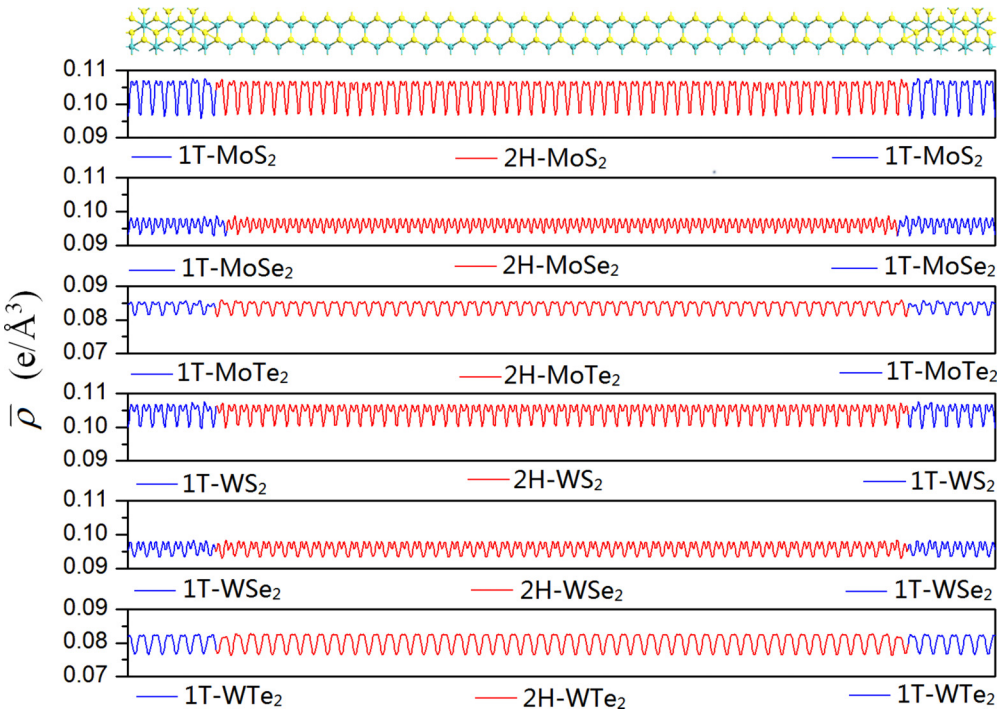

FIG. 3. The average electron density values along the *Z* direction of six TMDs monolayer junctions. The 1*T*-2*H*-1*T*MoS_2 device is also demonstrated as a schematic structure on the top of the figure.

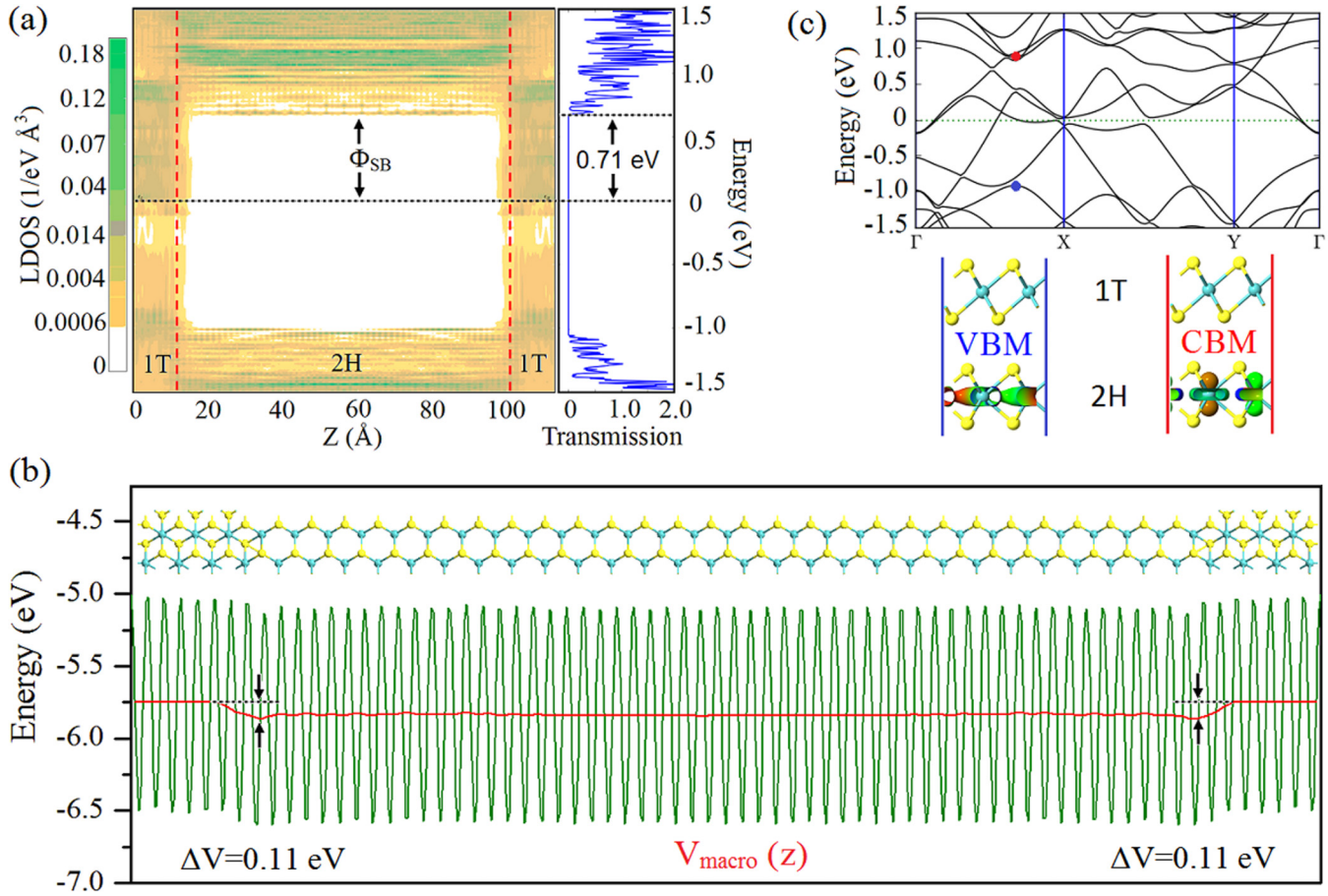

FIG. 4. (a) LDOS and transmission spectrum of the 1T-2H-1TMoS$_2$ system under zero-bias voltage. The Fermi energy is set to zero in the energy scale. (b) The averaged potential along the Z direction (in turquoise) and the macroscopic average potential V_{macro} (z) (in red) of the 1T-2H-1TMoS$_2$ system under zero-bias voltage. (c) Electronic band structure of OP MoS$_2$-1T/MoS$_2$-2H contact with interlayer distance 3.0 Å. The Fermi energy is set to zero in the energy scale. The VBM and CBM of the MoS$_2$-2H are marked by blue and red dots. Isosurfaces show the spatial distributions of the Bloch states of VBM and CBM, respectively.

level (FL) of 1T-MoS$_2$ and the conduction band minimum (CBM) of the 2H-MoS$_2$ in the local density states (LDOS) or the transmission spectrum. The value is 0.71 eV. Then, we calculate its averaged potential along the Z direction and the macroscopic average potential $V_{\text{macro}}(z)$ under zero-bias voltage. This way, the linear variation of $V_{\text{macro}}(z)$ at the boundaries is reflected to linear band bending ($\Delta V = 0.11$ eV). Last, we get the real Schottky-barrier height at the 1T/2H interface. The Schottky-barrier height we obtained is a little different from the *ab initio* simulated result [30]. The main reason is the difference of the 1T/2H contact structure, which leads to different potential at the interface. The values of the IP-Φ_{SB} for six TMD-SBFETs are shown in Table I. We found that all the contacts are Schottky-barrier (SB) contacts with the 1T-FL located within the 2H band gap. The trend of the IP-Φ_{SB} follows that of the band gaps: the smaller E_g corresponds to smaller IP-Φ_{SB}. For comparison, the Schottky-barrier heights of the six OP 1T/2H contacts (OP-Φ_{SB}) are also calculated, which can be estimated by measuring the energy difference between 1T-FL and the CBM level in the 2H phase in Fig. 4(c) [13]. The interlayer distances are determined by minimizing the total energy. The OP-Φ_{SB} of OP 1T/2H contact is also shown in Table I, which is in line with the results obtained by Liu and Wei [13]. We see that the OP 1T/2H contact has slightly larger Φ_{SB} than that of IP-Φ_{SB}. This is because the interlayer interaction can redistribute the charge density at the interface and give rise to an interface dipole between 1T/2H in the OP heterostructure, and thus change the band alignment when the 1T and 2H layers become close to each other [13]. But in an IP heterostructure, it is only possible to form a dipole line at the junction, which is not enough to change the alignment further away from the junction.

Having studied the physics of band alignments for the 1T/2H heterojunction, we next simulate the current transfer characteristics of the device in Fig. 1(b) by using the NEGF method. Note that the Poisson equation is used to solve the potential profiles in the TMDs channel region for a given bias situation. Figure 5(a) depicts the I-V characteristics of six IP TMD-SBFETs with 8.8 nm physical gate length. V_{DD} and EOT follow the ITRS HP 2022. The first question for the SBFET is whether the subthreshold swing (SS), which is the gate voltage needed to change the current by a factor of 10, can be close to its thermal-dynamic limit of 60 meV. In a SBFET, the barrier is not at the center of the channel, instead it is at the SB itself. Although the barrier height Φ_{SB} itself

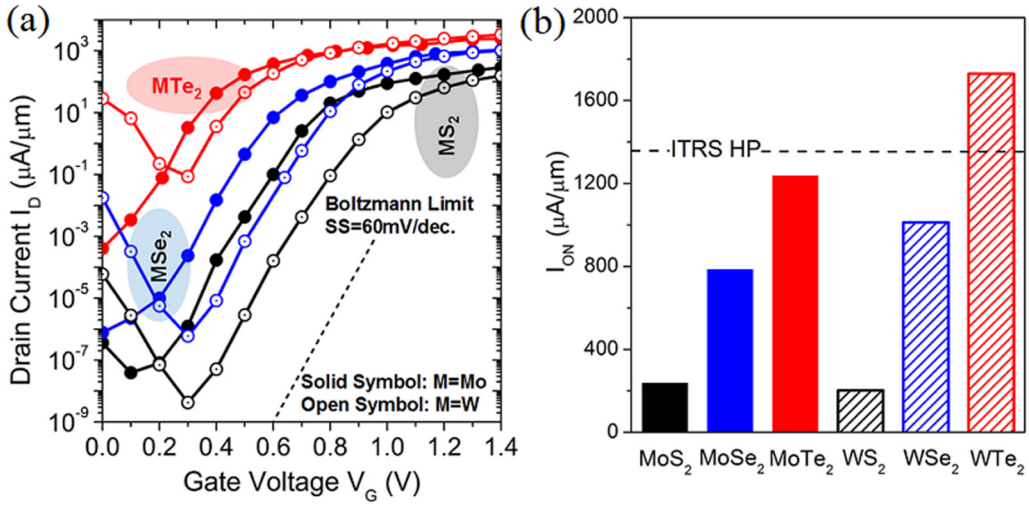

FIG. 5. (a) Transfer characteristics of MoX_2-SBFETs (solid symbol) and WX_2-SBFETs (open symbol) with 8.8 nm physical gate length (X = S,Se,Te). The dashed black line is the Boltzmann's thermal limit. (b) ON currents of six TMD-SBFETs. I_{ON} of the ITRS HP requirement is indicated by the dashed black line.

will not change with the changing gate voltage, the potential profile at the other side of the SB will be changed by the gate voltage. This can change the SB thickness at a given energy level. If smaller than a given thickness, the tunneling becomes very efficient (say close to 1), so the distance from the source Fermi energy to this energy level (which has the critical tunneling thickness) will become the effective barrier. This barrier can be controlled by the gate voltage. Nevertheless, due to such indirect relationship, the SBFFT usually has larger SS than the thermal-dynamic limit. This can be illustrated by an approximation formula for SBFET: $SS = a_{SB}(kT/q)\ln(10)$, where $a_{SB} = 1/[1 - \exp(-d_{tunn}/\lambda)]$ [36,37], d_{tunn} is the SB thickness when the tunneling become very large, and λ is an equivalent vertical thickness of the tunneling layer. Due to a_{SB}, the SS of a SBFFT is always larger than the ideal thermal-dynamic limit of $(kT/q)\ln(10)$. Note that our simulation does not rely on this approximated formula; instead it includes all tunneling and thermal distribution effects in the calculation. From our simulated results shown in Fig. 5(a), it is found that the SS's for all the TMD materials are close to the thermal-dynamic limit. This is mostly because of the thin vertical direction layers of TMD and oxides (∼1–2 nm) and the relatively large d_{tunn}(∼6−7 nm). This shows the true advantages of using 2D materials for FET: the efficient control of the channel potential through the gate voltage due to the thin vertical thickness.

We next consider the on-state current I_{ON}, which is often a problem for 2D FET due to the thin atomic monolayer of the channel. The maximal drain current is inversely proportional to the Schottky-barrier height. Indeed, due to the smallest Φ_{SB}, the I_{ON} is biggest for WTe_2-SBFET. All the I_{ON} currents are illustrated in Fig. 5(b). Here, I_{ON} is defined as the current corresponding to the gate voltage of $V_{ON} = V_{OFF} + V_{DD}$ (V_{OFF} is the gate voltage of I_{OFF} as 0.1 μA/μm). From the figure, one can see that I_{ON} is inversely correlated with the Schottky-barrier height. The ON currents of MoS_2-SBFET and WS_2-SBFET fall far below the ITRS HP requirement (1350 $\mu A/\mu m$) due to the large Φ_{SB}. Only the I_{ON} of WTe_2-SBFET, being at 1729 $\mu A/\mu m$, is higher than the ITRS HP requirement. Thus, although the SBFET in Ref. [21] was synthesized with MoS_2, we suggest that if the same SBFET can be synthesized with WTe_2 in the future, the performance could be much better (increase I_{ON} by a factor of 7).

To reveal the origins for the superior performance of WTe_2-SBFET, we performed analyses on the LDOS at the OFF state ($V_G = 0.3$ V) and the ON state ($V_G = 1.02$ V) in Figs. 6(a) and 6(b). When the gate voltage is applied, the CBM of the 2H-channel region will move down gradually. At $V_G = 0.30$ V, the drain current is minimum at I_{OFF} (0.1 $\mu A/\mu m$). A large triangular Schottky barrier in Fig. 6(a) is formed due to the shift down of central LDOS, which prevents the current from tunneling through. This can also be illustrated by the transmission eigenstates at the FL of the source ($E = 0.35$ eV) in Fig. 6(c). We found that the incoming wave functions of two eigenstates, $E1$ and $E2$, all localize on the sources and are unable to go through the central channel to reach the drain. When the gate voltage further increases, the CBM of the center 2H channel will decrease and bypass the FL of the 1T source region, and turn on the transistor. At $V_G = 1.02$ V, the Schottky barrier in Fig. 6(b) becomes much thinner and the direct tunneling through the barriers dominates the drain currents. In Fig. 6(d), the incoming wave functions of two eigenstates, $E1$ and $E2$, delocalize over the whole device, including the central channel and drain. Moreover, the spatial distributions of the eigenstates indicates the electron tunneling through the device mainly localizes on the transition metal (Mo or W).

Finally, we compare the IP-SBFET with the more traditional OP-SBFET with 8.8 nm 2H-WTe_2 as the channel and both using 1T-WTe_2 as the source and drain electrodes. The use of the same electrode provides a more controlled comparison. Due to the contact edge effect, increasing the overlapping area will not necessarily improve the contact. Thus, we have overlapped the 2H-WTe_2 and 1T-WTe_2 with 1 nm length. EOT and V_{DD} are the same as that of IP-SBFET. The calculated I/V curve for this OP-SBFET is shown in Fig. 7(a)

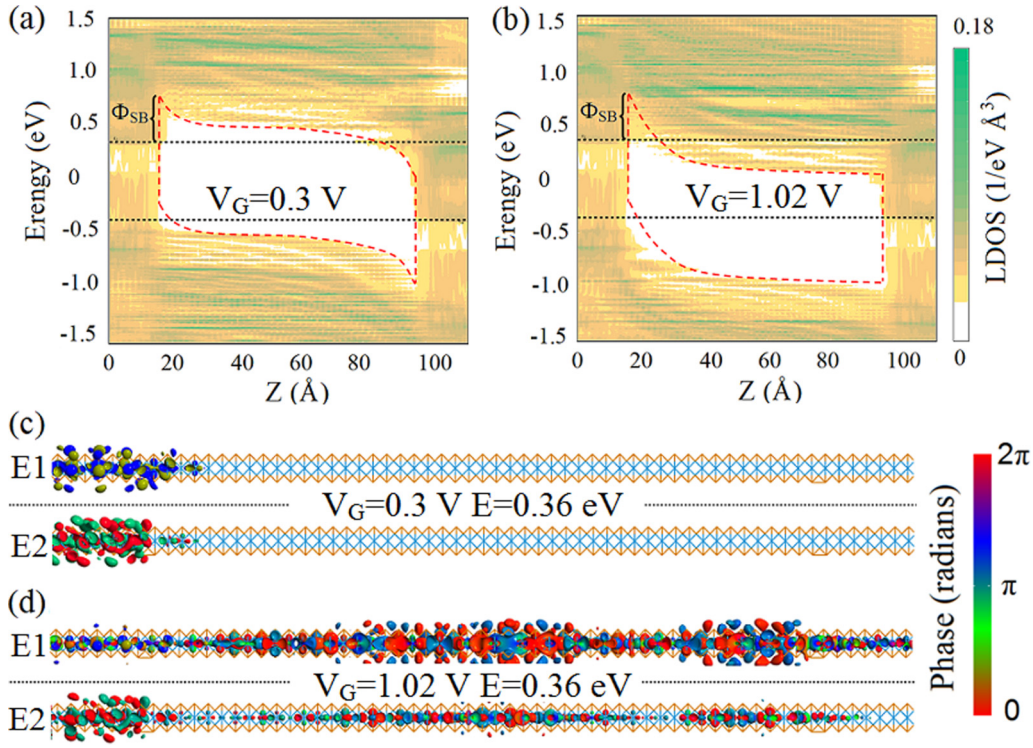

FIG. 6. LDOS of WTe_2-SBFET at (a) the OFF state and (b) the ON state. Upper and lower black dashed lines indicate the FL of the source and drain. Red dashed lines represent the schematic view of the band profile of the SBFETs. Two transmission eigenstates, $E1$ and $E2$, at the FL of the source of the (c) OFF state and the (d) ON state. The isovalues are fixed at 0.2 for all eigenstates.

in comparison with that of the IP-SBFET. We see that the performance of OP-SBFET is significantly worse than that of IP-SBFET. Not only does it have lower I_{ON}, but its SS is also larger. This is because, in the OP-SBFET, the tunneling happens at the horizontal interface area between $2H$-WTe_2 and $1T$-WTe_2, and this region is outside the potential control area of the gate. Thus a short-channel effect exists, which increases the SS. On the other hand, for IP-SBFET, the tunneling place is at the edge of the gate; it is under the effective control of the gate. The smaller I_{ON} (by a factor of 4) for OP-SBFET comes from the large resistance of the current. Not only is the OP-Φ_{SB} slightly larger, but the wave-function coupling between the $1T$ layer and $2H$ layer is also weaker since the electron in the $2H$ phase is localized at the inside layer of W, as can be seen clearly in Figs. 7(b) and 7(c). At the OFF state, the incoming wave functions of two eigenstates, $E1$ and $E2$, all localize on the sources and the far left of $2H$-WTe_2. When the gate voltage increases to 1.0 V, the incoming wave functions of the first eigenstate delocalize over the whole device including the central channel and drain. But the incoming wave functions of the second eigenstate just spread to the central channel and do not reach the drain. In contrast to all of the above, in the IP $1T/2H$ heterojunction, the coupling is due to covalent bonding and can happen at the inside layer, thus it can be much stronger.

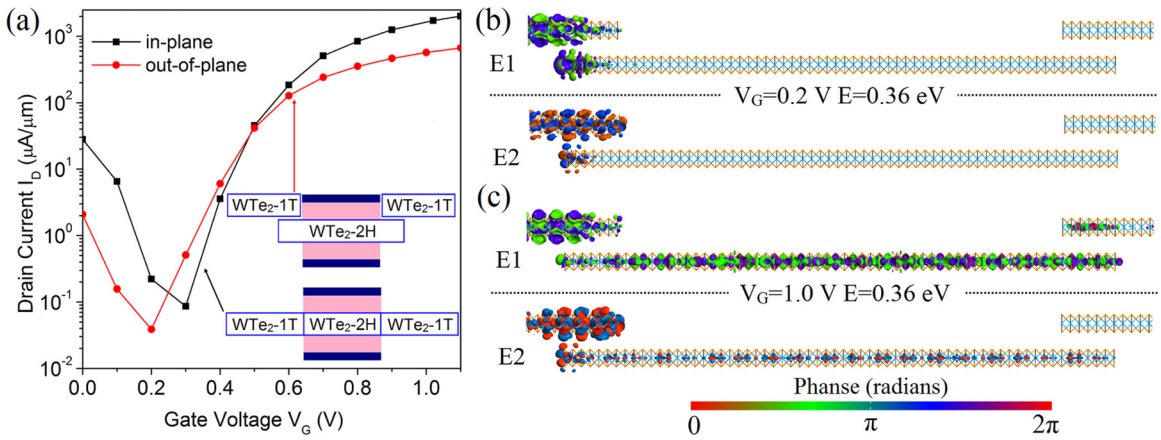

FIG. 7. (a) Transfer characteristics of IP WTe_2-SBFET and OP WTe_2-SBFET with 8.8 nm physical gate length. Two transmission eigenstates, $E1$ and $E2$, at the FL of the source of (b) the OFF state and (c) the ON state. The isovalues are fixed at 0.2 for all eigenstates.

IV. CONCLUSION

In conclusion, we have investigated the band alignment of the $1T/2H$ heterjunction, both for IP and OP structures, and we have also simulated the performance of the corresponding single-layer IP-SBFET. Our study shows that the Φ_{SB} of the in-plane $1T/2H$ contacts are smaller than the Φ_{SB} of out-of-plane contacts, and the contact coupling is also stronger in the IP case. We found that if the WTe_2 is used, the I_{ON} can be higher than the ITRS requirement for sub-10-nm devices. We also show that the IP heterostructure is indeed a better arrangement compared to the OP counterpart. Not only is its SS smaller and close to the thermal-dynamic limit, but its I_{ON} is also much bigger. This is due to the effective control of the potential at the tunneling area of the Φ_{SB} in the IP arrangement, and stronger coupling of the $1T$, $2H$ wave functions. Overall, our study shows that WTe_2 $1T/2H$ IP-SBFET could be a viable sub-10-nm single-layer device.

ACKNOWLEDGMENTS

This work was supported by the National Natural Science Foundation of China (Grants No. 11674039, No. 11574304, and No. 11774338), the China Postdoctoral Science Foundation (Grant No. 2016M601099), and the Scientific Research Fund of Hunan Provincial Education Department (Grant No. 15A004). X.W.J. acknowledges the support of this work by the Youth Innovation Promotion Association CAS (Grant No. 2016109) and Chinese Academy of Sciences-Peking University Pioneer Cooperation Team (CAS-PKU Pioneer Cooperation Team). L.W.W. is supported by the Director, Office of Science (SC), Basic Energy Science (BES), Materials Science and Engineering Division (MSED), of the U.S. Department of Energy (DOE) under Contract No. DE-AC02-05CH11231 through the Material Theory Program (KC2301).

[1] D. Xiang, H. Jeong, T. Lee, and D. Mayer, Adv. Mater. **25**, 4845 (2013).
[2] A. D. Franklin, Science **349**, 2750 (2015).
[3] D. Xiang, X. L. Wang, C. C. Jia, T. Lee, and X. F. Guo, Chem. Rev. **116**, 4318 (2016).
[4] Z. Li, J. X. Zheng, Z. Y. Ni, R. G. Quhe, Y. Y. Wang, Z. X. Gao, and J. Lu, Nanoscale **5**, 6999 (2013).
[5] X. S. Wang, H. B. Feng, Y. M. Wu, and L.Y. Jiao, J. Am. Chem. Soc. **135**, 5304 (2013).
[6] X. W. Jiang and S. S. Li, Appl. Phys. Lett. **104**, 193510 (2014).
[7] Y. H. Zhou, J. Zeng, and K. Q. Chen, Carbon **76**, 175 (2014).
[8] Á. Szabó, R. Rhyner, and M. Luisier, Phys. Rev. B **92**, 035435 (2015).
[9] Y. P. An, M. J. Zhang, D. P. Wu, Z. M. Fu, and K. Wang, J. Mater. Chem. C **4**, 10962 (2016).
[10] X. K. Chen, Z. X. Xie, W. X. Zhou, L. M. Tang, and K. Q. Chen, Appl. Phys. Lett. **109**, 023101 (2016).
[11] K. F. Mak, C. Lee, J. Hone, J. Shan, and T. F. Heinz, Phys. Rev. Lett. **105**, 136805 (2010).
[12] C. H. Chang, X. F. Fan, S. H. Lin, and J. L. Kuo, Phys. Rev. B **88**, 195420 (2013).
[13] Y. Y. Liu, P. Stradins, and S. H. Wei, Sci. Adv. **2**, 1600069 (2016).
[14] X. W. Jiang, J. Gong, N. Xu, S. S. Li, J. F. Zhang, Y. Hao, and L. W. Wang, Appl. Phys. Lett. **104**, 023512 (2014).
[15] J. H. Kang, W. Liu, D. Sarkar, D. Jena, and K. Banerjee, Phys. Rev. X **4**, 031005 (2014).
[16] Y. Y. Wang, R. X. Yang, R. G. Quhe, H. X. Zhong, L. X. Cong, M. Ye, Z. Y. Ni, Z. G. Song, J. B. Yang, J. J. Shi, J. Li, and J. Lu, Nanoscale **8**, 1179 (2016).
[17] S. Das, H. Y. Chen, A. V. Penumatcha, and J. Appenzeller, Nano Lett. **13**, 100 (2013).
[18] M. Buscema, M. Barkelid, V. Zwiller, H. S. J. van der Zant, G. A. Steele, and A. Castellanos-Gomez, Nano Lett. **13**, 358 (2013).
[19] C. Ataca, H. Şahin, and S. Ciraci, J. Phys. Chem. C **116**, 8983 (2012).
[20] K. A. N. Duerloo, Y. Li, and E. J. Reed, Nat. Commun. **5**, 4214 (2014).
[21] K. C. Santosh, C. X. Zhang, S. Hong, R. M. Wallace, and K. Cho, 2D Mater. **2**, 035019 (2015).
[22] A. Singh, S. N. Shirodkar, and U. V. Waghmare, 2D Mater. **2**, 035013 (2015).
[23] M. Calandra, Phys. Rev. B **88**, 245428 (2013).
[24] T. Hu, R. Li, and J. Dong, J. Chem. Phys. **139**, 174702 (2013).
[25] D. B. Putungan, S. H. Lin, and J. L. Kuo, Phys. Chem. Chem. Phys. **17**, 21702 (2015).
[26] A. Ambrosi, Z. Sofer, and M. Pumera, Chem. Commun. **51**, 8450 (2015).
[27] S. S. Chou, Y. K. Huang, J. Kim, B. Kaehr, B. M. Foley, P. Lu, C. Dykstra, P. E. Hopkins, C. J. Brinker, J. X. Huang, and V. P. Dravid, J. Am. Chem. Soc. **137**, 1742 (2015).
[28] Y. S. Guo, D. Z. Sun, B. Ouyang, A. Raja, J. Song, T. F. Heinz, and L. E. Brus, Nano Lett. **15**, 5081 (2015).
[29] F. Güller, A. M. Llois, J. Goniakowski, and C. Noguera, Phys. Rev. B **91**, 075407 (2015).
[30] Y. Katagiri, T. Nakamura, A. Ishii, C. Ohata, M. Hasegawa, S. Katsumoto, T. Cusati, A. Fortunelli, G. Iannaccone, G. Fiori, S. Roche, and J. Haruyama, Nano Lett. **16**, 3788 (2016).
[31] R. Kappera, D. Voiry, S. E. Yalcin, B. Branch, G. Gupta, A. D. Mohite, and M. Chhowalla, Nat. Mater. **13**, 1128 (2014).
[32] Y. Q. Ma, B. L. Liu, A. Y. Zhang, L. Chen, M. Fathi, C. F. Shen, A. N. Abbas, M. Y. Ge, M. Mecklenburg, and C. W. Zhou, ACS Nano. **9**, 7383 (2015).
[33] M. Brandbyge, J. L. Mozos, P. Ordejón, J. Taylor, and K. Stokbro, Phys. Rev. B **65**, 165401 (2002).
[34] M. Büttiker, Y. Imry, R. Landauer, and S. Pinhas, Phys. Rev. B **31**, 6207 (1985).
[35] M. Aras, Ç. Kılıç, and S. Ciraci, Phys. Rev. B **95**, 075434 (2017).
[36] J. Knoch, M. Zhang, S. Mantl, and J. Appenzeller, IEEE Trans. Elect. Dev. **53**, 1669 (2006).
[37] M. Zhang, J. Knoch, J. Appenzeller, and S. Mantl, IEEE Elect. Dev. Lett. **28**, 223 (2007).